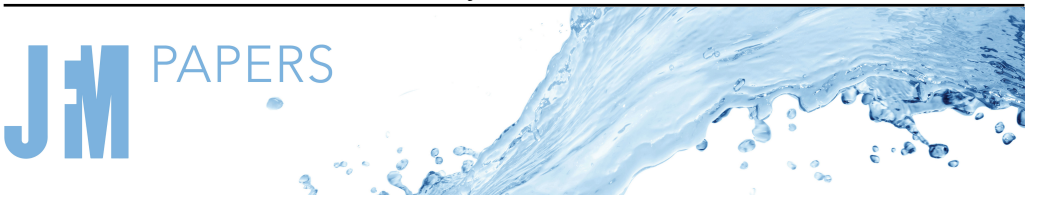
J. Fluid Mech. (2026), *vol.* 1043, A20, doi:10.1017/jfm.2026.12044



Self-consistent fragmentation in dynamically dense turbulent fibre suspensions

Andrea Mazzino[1,2], **Dandan Xiao**[3], **Lu Rongpei**[3] and **Xuerui Mao**[4,5]

[1]Department of Civil, Chemical and Environmental Engineering (DICCA), University of Genoa, Via Montallegro 1, Genova 16145, Italy

[2]INFN, Genova Section, Via Dodecaneso 33, Genova 16146, Italy

[3]School of Aerospace Engineering, Beijing Institute of Technology, Beijing 100081, PR China

[4]Beijing Institute of Technology (Zhuhai), Zhuhai, 519088, PR China

[5]State Key Laboratory of Explosion Science and Safety Protection, Beijing 100081, PR China

Corresponding authors: Andrea Mazzino, andrea.mazzino@unige.it; Dandan Xiao, dxiao@bit.edu.cn

(Received 27 February 2026 UTC; revised 20 July 2026 UTC; accepted 13 August 2026 UTC)

Fragmentation of slender fibres by turbulence controls length distributions in many natural and industrial suspensions, yet most theories assume a prescribed carrier flow, and treat fibres as dilute and dynamically passive. Here, we develop a self-consistent kinetic description for fragmentation in the opposite limit of sufficiently dense fibre suspensions that back-react on the turbulence. Starting from an Euler–Bernoulli model in the quasi-static regime, we show that collective resistive-force drag defines a cut-off span L_c inside the inertial range, marking the crossover from a Kolmogorov-like inertial range with an effective linear friction (for scales above L_c) to a fibre-dominated frictional regime with $E(k) \propto k^{-3}$ for scales below L_c. In this regime, the curvature amplitude of an almost straight fibre rises steeply with its span, so that the supercritical breaking hazard loses its dependence on length, and approaches a plateau controlled solely by the fibre loading. Embedding this hazard into a scale-invariant binary fragmentation equation, adopted here as a minimal quasi-static closure, we obtain, without adjustable parameters, a corresponding asymptotic steady length spectrum $n(L) \propto L^{-2}$ in the fibre-dominated regime, in contrast with the shallower $L^{-4/3}$ law predicted in the Kolmogorov-like regime. The crossover between these two spectra is set self-consistently by the same length density that fixes L_c and the onset of the frictional modification of the cascade, thus linking turbulence modification, curvature statistics and kinetic fragmentation in a single coupled framework.

Key words: isotropic turbulence, homogeneous turbulence, suspensions

© The Author(s), 2026. Published by Cambridge University Press. This is an Open Access article, distributed under the terms of the Creative Commons Attribution licence (https://creativecommons.org/licenses/by/4.0/), which permits unrestricted re-use, distribution and reproduction, provided the original article is properly cited.

https://doi.org/10.1017/jfm.2026.12044 Published online by Cambridge University Press

1. Introduction

Slender fibres fragmented by turbulence are ubiquitous in nature and technology, from cellulosic and textile microfibres in the ocean surface layer (Ryan *et al.* 2020; Suaria *et al.* 2020*a*,*b*; Mazzino & Suaria 2026) to fibre-reinforced suspensions in process engineering, such as papermaking and biomass-conversion flows (Derakhshandeh *et al.* 2011; Lundell *et al.* 2011; Khan *et al.* 2023). In all these settings, the fragmentation statistics control key macroscopic properties as light scattering and biofilm colonisation in the environment. Understanding how turbulence bends, stretches and eventually breaks fibres, and how this translates into a steady length distribution, is therefore an issue of paramount importance.

Over the past decade, much progress has been made on the dynamics of fibre suspensions in turbulence (Chiarini *et al.* 2024; Marchioli *et al.* 2026). Direct numerical simulations (DNS) by Allende *et al.* (2018, 2020) have clarified how sub-Kolmogorov slender fibres are stretched and intermittently buckled by homogeneous isotropic turbulence, and how brittle inextensible fibres break by tensile and flexural failure, yielding fragmentation rates and daughter-size distributions. Laboratory experiments and simulations by Gay *et al.* (2018) have characterised the curvature statistics and conformational regimes of flexible fibres in turbulence, while classical theory by Olson & Kerekes (1998), pioneering experiments by Parsa & Voth (2014), and later work by Bounoua *et al.* (2018) have clarified the rotation and inertial tumbling of long rigid fibres. In a different setting, Singh *et al.* (2022) have shown how turbulence modifies the sedimentation and tumbling of long elastic filaments.

A complementary line of work has focused on turbulence-driven fragmentation of other deformable objects. Brouzet *et al.* (2021) proposed a laboratory model for plastic filament fragmentation in a turbulent von Karman flow, combining experiments and simulations to infer curvature-based breaking criteria and daughter-length distributions in the inertial range. Together with classical fragmentation models, which relate prescribed size-dependent breaking rates and kernels to power-law fragment spectra (Ziff & McGrady 1985; Krapivsky & Ben-Naim 1994; Domokos *et al.* 2015), these studies motivate a kinetic description of fibre lengths in terms of a break-up hazard inherited from the turbulent forcing. Recently, Mazzino (2026*b*) developed such a turbulence-informed kinetic theory for slender fibres in the dilute, one-way coupled regime: starting from an Euler–Bernoulli beam forced by inertial-range eddies, that work derives curvature-based hazards with distinct supercritical branches above and below a turbulence-defined critical span, and obtains self-similar binary fragmentation spectra that quantitatively account for the observed length distributions of environmental microfibres. For a recent perspective discussing the emergence (and limitations) of power-law fragment-size distributions under maximal-randomness arguments, see Villermaux (2025).

In parallel, a substantial effort has been devoted to understanding how fibres feed back on turbulent flows. The DNS of turbulence in a network of fixed rigid fibres (Olivieri *et al.* 2020*a*) and in suspensions of moving rigid fibres (Olivieri *et al.* 2020*b*) have shown that fibre drag can deplete large-scale kinetic energy, acting as an effective Darcy-type linear friction accompanied by non-Kolmogorov small-scale fluctuations. Fully coupled simulations of finite-size flexible fibres (Olivieri *et al.* 2022) demonstrate that fibre loading, stiffness and aspect ratio can substantially alter energy transfer, dissipation and coherent structures in homogeneous turbulence. These results are synthesised in recent reviews on finite-size fibre-like objects in turbulent flows (Chiarini *et al.* 2024; Marchioli *et al.* 2026), which also report on fibre-based diagnostics where fibre back-reaction on the flow is negligible in Rosti *et al.* (2018) and Brizzolara *et al.* (2021), but dynamically relevant in the fully coupled setting of Olivieri *et al.* (2022).

https://doi.org/10.1017/jfm.2026.12044 Published online by Cambridge University Press

Taken together, these lines of research have clarified many aspects of fibre dynamics and fragmentation in turbulence, but they also reveal a persistent gap. Dilute, one-way coupled theories, including the kinetic framework of Mazzino (2026*b*), treat the turbulent statistics as an input, and predict the breaking hazard and length spectrum from it, ignoring the effect of fibre loading on the flow. Fully coupled simulations of dense fibre suspensions demonstrate that fibres can qualitatively modify the turbulent cascade (Olivieri *et al.* 2020*a*,*b*), yet they do not offer a quantitative explanation for the resulting k^{-3} energy spectrum, and in turn, on how the modified fluctuations feed back onto fragmentation kinetics and the resulting length distribution.

The goal of this work is to fill that gap by developing a first kinetic theory of fibre fragmentation in dynamically dense turbulent fibre suspensions. The central result is that fibre drag produces two distinct inertial-range scaling regimes. When fibre feedback is weak, the turbulence remains close to the Kolmogorov $k^{-5/3}$ spectrum, and the associated fragmentation cascade leads to a length distribution $n(L) \propto L^{-4/3}$, in line with classical one-way coupled theories. When fibre drag becomes the dominant small-scale sink of energy, the spectrum steepens towards k^{-3}, and the kinetic description predicts a correspondingly steeper branch $n(L) \propto L^{-2}$ for shorter fibres. The crossover between these two scaling regimes is determined self-consistently by the global fibre loading, through a cut-off length L_c that marks the scale at which collective fibre drag balances inertial transfer, thus linking turbulence modification and fragmentation kinetics within a single framework.

The paper is organised according to this causal chain. In § 2, we first specify the quasi-static single-fibre model and the span-scale forcing needed to define the hydrodynamic feedback. In § 3, we briefly show that the quasi-static assumption is relevant for oceanic microfibres, while making clear that this environmental estimate concerns the fibre response, not the dynamically dense condition. In § 4, we then use the same span-scale drag closure to derive the collective cut-off L_c and the carrier-flow spectrum, including the fibre-dominated k^{-3} branch. Only after the carrier flow has been determined do we return, in §§ 5 and 6, to the consistency of the quasi-static regime and to the resulting curvature and hazard scalings. The available numerical and experimental evidence is discussed in § 7, with the quantitative carrier-flow comparison to Olivieri *et al.* (2022) given in § 7.3. Finally, § 8 inserts the resulting hazards into the binary fragmentation kinetics.

2. Set-up and dilute quasi-static regime

We consider a slender inextensible fibre of length L and radius a, and bending rigidity γ, embedded in homogeneous, isotropic turbulence of a Newtonian fluid with density ρ and kinematic viscosity ν. The turbulence is maintained in a statistically steady state by forcing at an injection scale L_{inj}, the largest scale of the problem, and has mean dissipation rate ε. The Kolmogorov length is $\eta \equiv (\nu^3/\varepsilon)^{1/4}$ (Frisch 1995).

The fibre is modelled as a neutrally buoyant Euler–Bernoulli beam with aspect ratio $a/L \ll 1$, subject to a transverse hydrodynamic force per unit length f_h described by resistive-force theory (RFT) (Batchelor 1970; Cox 1970; Kim & Karrila 1991; du Roure *et al.* 2019). At the level of scalings, we write

$$f_h \sim \xi_\perp u_L, \tag{2.1}$$

where u_L is the velocity increment across the fibre span L, and $\xi_\perp$ is the transverse drag coefficient.

Figure 1 summarises the fibre geometry and the span-scale forcing used in the quasi-static (QS) closure.

https://doi.org/10.1017/jfm.2026.12044 Published online by Cambridge University Press

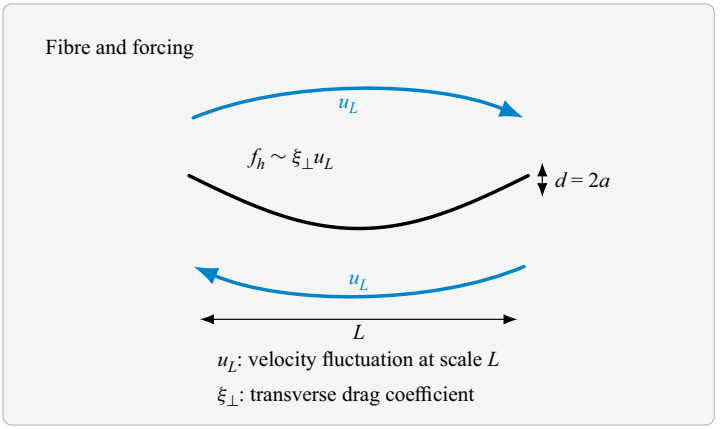


Figure 1. Slender-fibre geometry and span-scale forcing used in the QS closure. The fibre has span L, radius a, bending rigidity γ, and transverse drag coefficient $\xi_\perp$. A turbulent velocity increment u_L across the fibre span produces a transverse hydrodynamic load $f_h \sim \xi_\perp u_L$.

The effective relative velocity entering (2.1) should not be interpreted as a particle-like inertial or buoyancy-driven slip. In a strictly uniform flow, the leading-order transverse loading would indeed vanish. Here, however, the fibre is an extended, inextensible object immersed in a non-uniform carrier flow, so the relevant forcing is set by the velocity increment across its span. Even for a neutrally buoyant fibre, the ambient velocity field sampled along the fibre is not, in general, kinematically compatible pointwise with the instantaneous motion of a connected slender body. The resulting mismatch generates the distributed hydrodynamic traction that is captured at the scaling level by (2.1). In this sense, the present mechanism is controlled by span-L velocity differences, consistently with the inertial-range fibre-as-probe viewpoint discussed by Rosti *et al.* (2018) and Brizzolara *et al.* (2021), and not by the buoyancy-induced slip relevant e.g. in bubble-induced turbulence.

Equation (2.1) is therefore used here as a minimal slender-body scaling closure. The large Reynolds number of the carrier turbulence does not imply a similarly large Reynolds number for the local flow around the fibre cross-section, the relevant quantity being $Re_a \sim u_L a/\nu$ rather than $u_{inj}L_{inj}/\nu$, where u_{inj} is the typical large-scale velocity. In the slender limit $a \ll L$, an inertial-range carrier flow can thus coexist with a small local cross-sectional Reynolds number. Possible finite-Re_a corrections may modify order-one prefactors in $\xi_\perp$, but not the scaling role assigned here to the transverse loading $\xi_\perp u_L$.

We refer to the dynamically dilute regime (to be defined quantitatively later) as the case in which fibres exert negligible feedback on the flow and are well described by one-way coupling, so that the turbulence remains that of the bare flow (Frisch 1995). Namely,

$$u_L \sim (\varepsilon L)^{1/3}, \quad \tau_L \sim \varepsilon^{-1/3} L^{2/3}, \tag{2.2}$$

for the velocity increment and eddy turnover time across the fibre span. In the QS regime, the fibre responds as a static Euler–Bernoulli beam to the slowly varying load f_h. The midspan curvature then scales as (Mazzino 2026*b*)

$$\kappa_{QS}(L) \sim \frac{f_h L^2}{\gamma} \sim \frac{\xi_\perp}{\gamma}\,\varepsilon^{1/3} L^{7/3}, \quad (\kappa L)_{QS} \sim \frac{\xi_\perp}{\gamma}\,\varepsilon^{1/3} L^{10/3}. \tag{2.3}$$

Here and below, κ denotes a characteristic midspan/peak curvature amplitude, i.e. the quantity relevant for curvature-threshold exceedances, rather than a fibre-averaged mean

https://doi.org/10.1017/jfm.2026.12044 Published online by Cambridge University Press

curvature. The QS regime is such that the bending time $\tau_b(L) \sim \xi_\perp L^4/\gamma$ is short compared with the eddy time:

$$\tau_L \gg \tau_b(L), \quad \text{i.e.} \quad L \ll L_{QS} \equiv \left(\frac{\gamma\, \varepsilon^{-1/3}}{\xi_\perp}\right)^{3/10}. \tag{2.4}$$

Under this condition, the fibre is effectively slaved to the local flow.

Following the kinetic theory developed by Mazzino (2026*b*), we model break-up as a first-passage event associated with curvature-threshold exceedances over correlation blocks of duration of order τ_L. Let $p_b(L;\kappa_b)$ denote the probability that an intact fibre of span L breaks during one such block. Approximating successive blocks as weakly correlated Bernoulli trials, the probability that break-up occurs for the first time on the nth block is

$$\mathbb{P}(N=n) = \big[1 - p_b(L;\kappa_b)\big]^{n-1}\, p_b(L;\kappa_b), \quad n = 1, 2, \ldots, \tag{2.5}$$

so that N is geometrically distributed. Its mean is therefore

$$\langle N\rangle = \sum_{n=1}^{\infty} n\, \mathbb{P}(N=n) = p_b(L;\kappa_b) \sum_{n=1}^{\infty} n\big[1 - p_b(L;\kappa_b)\big]^{n-1}. \tag{2.6}$$

Introducing

$$q \equiv 1 - p_b(L;\kappa_b), \tag{2.7}$$

the sum in (2.6) is the derivative of the geometric series

$$\sum_{n=0}^{\infty} q^n = \frac{1}{1-q}, \quad \sum_{n=1}^{\infty} n q^{\,n-1} = \frac{1}{(1-q)^2}, \quad |q| < 1, \tag{2.8}$$

hence

$$\langle N\rangle = p_b(L;\kappa_b)\, \frac{1}{\big(1-q\big)^2} = p_b(L;\kappa_b)\, \frac{1}{p_b(L;\kappa_b)^2} = \frac{1}{p_b(L;\kappa_b)}. \tag{2.9}$$

The corresponding mean waiting time to break-up is then

$$\langle T(L)\rangle \sim \tau_L\, \langle N\rangle \sim \frac{\tau_L}{p_b(L;\kappa_b)}, \tag{2.10}$$

so that the coarse-grained hazard can be written as

$$h_0(L) \sim \frac{1}{\langle T(L)\rangle} \sim \frac{p_b(L;\kappa_b)}{\tau_L}. \tag{2.11}$$

In the supercritical regime $\kappa_b \lesssim \kappa_{QS}(L)$, threshold exceedance is a typical event over one correlation block, so $p_b(L;\kappa_b) = O(1)$ and carries no leading algebraic L-dependence (it tends to unity in the deeply supercritical limit). Hence

$$h_0(L) \sim \frac{1}{\tau_L} \sim \varepsilon^{1/3} L^{-2/3}, \quad \kappa_b \lesssim \kappa_{QS}(L), \tag{2.12}$$

up to order-one factors. By contrast, when $\kappa_b \gg \kappa_{QS}(L)$, one has $p_b \ll 1$, so the hazard is reduced by the stretched-exponential factor derived in Mazzino (2026*a*). In this sense, the hazard is the coarse-grained conditional break-up rate: the probability per unit time that a fibre of span L, still intact at the beginning of a correlation block, breaks before the next decorrelation event. This interpretation is valid as long as break-up can be treated as a

https://doi.org/10.1017/jfm.2026.12044 Published online by Cambridge University Press

first-passage event sampled over approximately independent blocks of duration τ_L; strong inter-block memory or correlated multi-break sequences would require a more detailed closure. In all regimes considered in this paper, we assume that the dynamics remains supercritical for the fibre lengths of interest.

3. Relevance of the QS regime for ocean microfibres

Before turning to dynamically dense suspensions, it is useful to note that the QS assumption is not merely a formal asymptotic limit for one of the environmental settings motivating this work. In their global survey of oceanic surface waters, Suaria *et al.* (2020*b*) found that most analysed fibres are cellulosic, with cotton being the most frequent single match. In the Southern Ocean subset, which includes the Antarctic Circumnavigation Expedition (ACE) sector, fibres have median length approximately 1 mm, and median diameter 16.7 μm, i.e. spans in the sub-millimetric to millimetric range, and diameters typical of textile microfibres.

Taking cotton as a representative of this dominant cellulosic fraction, and using a representative modulus $E \sim 5$–$10\,\mathrm{GPa}$ together with $a \simeq d/2 \simeq 8.35\ \mu\mathrm{m}$, one obtains a bending rigidity $\gamma \simeq E\pi a^4/4 \sim 2$–$4 \times 10^{-11}\,\mathrm{N\,m^2}$, typical of slender textile fibres. For the oceanic forcing, Derkani *et al.* (2021) report along the ACE a median wind speed $U_{10} = 7.25\,\mathrm{m\,s^{-1}}$, storm values up to 15–$20\,\mathrm{m\,s^{-1}}$, a median significant wave height $H_s = 2.61\,\mathrm{m}$, and mean wave periods typically in excess of 8 s. Inferring the near-surface turbulence level through the same friction-velocity route used in the ACE analysis, with $C_D = 1.3 \times 10^{-3}$, one obtains $u_{*w} \simeq 9 \times 10^{-3}\,\mathrm{m\,s^{-1}}$. Evaluating the wave-affected dissipation estimate $\varepsilon(z) \simeq \xi u_{*w}^3/(\kappa z)$ at a representative upper-decimetre depth $z \simeq 0.2\,\mathrm{m}$, with $\xi = 20$–100, then gives $\varepsilon \sim 2 \times 10^{-4}$–$10^{-3}\,\mathrm{m^2\,s^{-3}}$ under median ACE conditions. With the slender-body estimate $\xi_\perp \sim 4\pi\mu/\ln(L/a) = 4\pi\rho\nu/\ln(L/a)$, using $\mu \simeq 1.5 \times 10^{-3}\,\mathrm{Pa\,s}$, (2.4) then yields L_{QS} of several millimetres, typically $L_{QS} \sim$ 7–11 mm for the parameter range above. This remains safely above the characteristic sub-millimetric to millimetric spans of the dominant cotton-like microfibres reported by Suaria *et al.* (2020*b*), indicating that the QS modelling adopted here is realistic at least at the order-of-magnitude level for environmentally relevant ocean microfibres. Because $L_{QS} \propto \varepsilon^{-1/10}$, even scaling the median ACE estimate up to storm conditions would only reduce the threshold to a few millimetres.

We stress that this estimate concerns only the material and kinematic validity of the QS approximation. It is not meant to imply that open-ocean microfibre concentrations are necessarily dynamically dense in the sense of the next section.

4. Collective drag and the emergence of a cut-off length

We now increase the fibre concentration while keeping the fibres slender and non-aggregated. Let $n(L')$ denote the number density (per unit volume) of fibres with lengths in $(L', L' + \mathrm{d}L')$, supported on $(0, L_{max})$, where L_{max} is the maximal fibre length present in the suspension. The total fibre length per unit volume is

$$\mathcal{L} \equiv \int_0^{L_{max}} L'\, n(L')\, \mathrm{d}L'. \tag{4.1}$$

The quantity $\mathcal{L}$ has the dimensions of an inverse area, and represents the total fibre length per unit volume. This notation is the natural control variable of the collective-drag balance derived below. In the slender limit, it is directly related to the solid volume fraction through $\phi_V \sim \pi a^2 \mathcal{L}$, so working with $\mathcal{L}$ or ϕ_V amounts to the same information up to the constant

https://doi.org/10.1017/jfm.2026.12044 Published online by Cambridge University Press

geometric factor πa^2. Throughout, we allow $\mathcal{L}$ to vary over a wide range while keeping the solid volume fraction small, so that the suspension remains dilute in a volumetric sense (i.e. $\pi a^2 \mathcal{L} \ll 1$) but not necessarily in a dynamical sense as discussed below.

From (4.1), an eddy at scale r (roughly a cube of side r) therefore contains a total fibre length of order $\mathcal{L} r^3$. We have already seen that the hydrodynamic force per unit fibre length goes as $\xi_\perp u_r$, so that the total (dissipative) force exerted by the fibres on an eddy of size r (by Newton's third law) is $F_{drag}(r) \sim \xi_\perp u_r \, \mathcal{L} r^3$. Dividing by ρr^3, we immediately obtain a drag force density (force per unit mass)

$$\boldsymbol{f}_{drag}(r) \sim -\alpha \, \boldsymbol{u}_r, \quad \alpha \equiv \frac{\xi_\perp}{\rho} \mathcal{L}, \tag{4.2}$$

where we have assumed a homogeneous coarse-grained loading, so that the fibre length contained in an eddy of size r scales as $\mathcal{L} r^3$, together with orientation statistics broad enough for the drag to be treated as effectively isotropic. This is consistent with the broadly distributed orientations, despite preferential alignment with the eigenvectors of the local strain-rate tensor, reported in the DNS of Olivieri *et al.* (2022). More precisely, this effective isotropic closure is a mean-field closure over coarse-graining volumes of size r^3. It is intended for scales r at which the fibre population supplies many line elements sampling velocity fluctuations at that same scale. Equivalently, if the total fibre length in such a volume is $\mathcal{L} r^3$, then the number of independent line elements of extent r scales as $N_r \sim (\mathcal{L} r^3)/r \sim \mathcal{L} r^2$; hence the approximation is expected to be meaningful when $\mathcal{L} r^2 \gg 1$, i.e. for scales larger than the typical inter-fibre spacing $\mathcal{L}^{-1/2}$. Thus the use of u_r in the eddy-scale drag closure should not be read as the load on an individual fibre whose span is parametrically smaller than r, which would experience the eddy as nearly uniform. It is instead a coarse-grained estimate of the drag exerted by the fibre line density on velocity fluctuations at scale r. When the deformation and breaking of a fibre of span L are considered below, we set $r = L$, recovering the single-fibre forcing $f_h \sim \xi_\perp u_L$ introduced in (2.1).

The corresponding drag power per unit mass is

$$\varepsilon_{fib}(r) \sim \alpha \, u_r^2 \sim \frac{\xi_\perp}{\rho} \, \mathcal{L} \, u_r^2. \tag{4.3}$$

If $\mathcal{L}$ is sufficiently small that it does not alter the classical Kolmogorov (1941) (hereafter K41) cascade scenario (Frisch 1995), the inertial flux across scale r is $\Pi \sim u_r^3/r \sim \varepsilon$, and (4.3) is small compared with ε. As the length density $\mathcal{L}$ increases, there exists a scale $L_c \leq L_{inj}$ at which the fibre drag dissipation becomes comparable to the inertial flux:

$$\varepsilon_{fib}(L_c) \sim \varepsilon \quad \Leftrightarrow \quad \varepsilon \sim \frac{\xi_\perp}{\rho} \mathcal{L} \left(\varepsilon L_c\right)^{2/3}. \tag{4.4}$$

This yields the cut-off length

$$L_c \sim \left(\frac{\rho}{\xi_\perp \mathcal{L}} \, \varepsilon^{1/3} \right)^{3/2}. \tag{4.5}$$

As we will discuss in detail in § 7.3, fully coupled DNS by Olivieri *et al.* (2022) provide support for the existence of such a crossover in their QS-compatible branch.

Within this framework, dilute and dense acquire primarily dynamical meanings so that no fixed threshold in the geometric crowding number N_c (Kerekes & Schell 1992) can be singled out. We term suspensions dynamically dense when the crossover scale L_c, at which fibre drag balances the inertial energy flux, lies inside the inertial range, and dynamically dilute when it does not (i.e. $L_c > L_{inj}$). By simple manipulations, this

https://doi.org/10.1017/jfm.2026.12044 Published online by Cambridge University Press

condition can be recast in terms of a large-scale Stokes number, defined as $St_{inj} \equiv (\xi_\perp \mathcal{L}/\rho)\,\tau_{L_{inj}}$, with $\tau_{L_{inj}} \sim \varepsilon^{-1/3} L_{inj}^{2/3}$, for which $L_c/L_{inj} \sim St_{inj}^{-3/2}$. Dynamically dilute suspensions correspond to $St_{inj} \lesssim 1$ ($L_c \gtrsim L_{inj}$), whereas dynamically dense suspensions have $St_{inj} \gtrsim 1$, so that L_c lies within the inertial range. Thus the same suspension may remain geometrically dilute in the volumetric sense $\pi a^2 \mathcal{L} \ll 1$, while being dynamically dense, in the present sense, if the collective-drag crossover L_c falls inside the inertial range. We will be interested in the situation where

$$\eta \ll L_c \ll L_{inj} \quad \Leftrightarrow \quad 1 \ll St_{inj} \ll Re_{inj}^{1/2}, \qquad Re_{inj} \equiv \frac{u_{inj} L_{inj}}{\nu}. \tag{4.6}$$

The construction developed in this section is intentionally minimal. Above L_c, we retain only a Kolmogorov-like inertial-range input corrected by a coarse-grained linear drag, whereas below L_c, we seek only the dominant asymptotic balance between inertial transfer and collective fibre drag. The purpose is therefore to identify the relevant crossover scales and exponents, not to provide a detailed closure with predictive prefactors for all statistics of the modulated turbulence.

A natural realisation of the regime $\pi a^2 \mathcal{L} \ll 1$ but $St_{inj} = O(1)$ or larger is provided by very-low/low-consistency aqueous suspensions of millimetric cellulose or pulp fibres in papermaking headbox, white-water and de-inking flows (Derakhshandeh *et al.* 2011; Lundell *et al.* 2011). For representative $a \simeq 10$ μm and $\phi_V \simeq 10^{-4}$–10^{-3}, one obtains $\mathcal{L} \simeq \phi_V/(\pi a^2) \sim 3 \times 10^5$–$3 \times 10^6$ m^{-2}, so the cumulative drag can become dynamically relevant while the volume fraction remains small. Using the standard crowding number estimate $N_c \sim (2/3)\phi_V (L/d)^2$, with $d = 2a$ the fibre diameter (Kerekes & Schell 1992), millimetric fibres with $L/d \simeq 50$–100 remain well below the continuous-contact/network threshold over this range, although frequent collisions may occur at its upper end. Strongly flocculated, entangled or contact-dominated suspensions are outside the contact-free asymptotic setting considered here.

Figure 2 summarises the scale hierarchy and dominant balances associated with the dynamically dense regime.

4.1. *Large-scale fibre-drag-perturbed K41 inertial range*

For separations $L_c \ll r \ll L_{inj}$, the flow remains in a Kolmogorov-like inertial range, but the presence of the fibre population enters the coarse-grained Navier–Stokes dynamics as an effective Darcy-type linear friction term $-\alpha \boldsymbol{u}$, so that turbulence retains its scalings given by (2.2) with an attenuated energy flux set by a modified, fibre-controlled dissipation rate. Such a regime has already been observed by Olivieri *et al.* (2020*a*) in turbulence developing within a network of rigid, fixed fibres.

4.2. *Small-scale fibre-dominated frictional regime*

In the range $r \ll L_c$, we assume that viscous dissipation is subdominant (to be self-consistently checked *a posteriori*) and that at each scale r, the inertial transfer is locally balanced by drag on the fibres. This should be read as an asymptotic closure for a geometrically dilute yet dynamically dense suspension in which the cumulative back-reaction of the fibres can be represented, after coarse-graining, by an effective drag power linear in the span-scale relative velocity. At finite Reynolds number and for finite-size fibres, fully coupled DNS may display interphase transfer channels that appear non-local in spectral space (Olivieri *et al.* 2020*a*, 2022); the present point is that in the neutrally buoyant QS branch considered here, the same cumulative effect can be modelled at the scaling level by the simplest local drag closure. Under this assumption, stiffness and

https://doi.org/10.1017/jfm.2026.12044 Published online by Cambridge University Press

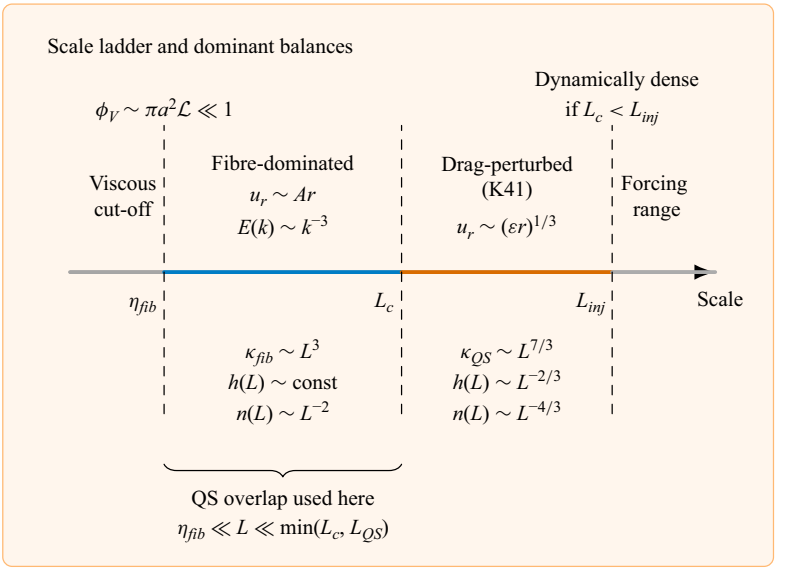


Figure 2. Scale ladder and dominant balances in the dynamically dense regime. The fibre-dominated interval $\eta_{fib} \ll r \ll L_c$ is characterised by $u_r \sim Ar$ and $E(k) \sim k^{-3}$, whereas the range $L_c \ll r \ll L_{inj}$ remains drag-perturbed Kolmogorov-like. The lower labels summarise the associated curvature, hazard and steady-fragment spectra used in the asymptotic theory.

aspect ratio mainly affect prefactors and regime boundaries through γ and $\xi_\perp$, whereas the exponent in the resulting scaling law is controlled by the linearity of the effective drag law. According to the present closure, the scale-by-scale energy balance reads

$$\frac{u_r^3}{r} \sim \varepsilon_{fib}(r) \sim \frac{\xi_\perp}{\rho}\,\mathcal{L}\,u_r^2. \tag{4.7}$$

Dividing by u_r^2 gives

$$\frac{u_r}{r} \sim A, \quad A \equiv \frac{\xi_\perp}{\rho}\mathcal{L}, \tag{4.8}$$

so that the velocity increments become linear in scale:

$$u_r \sim Ar, \quad r \ll L_c. \tag{4.9}$$

The associated eddy time is

$$\tau_r^{fib} \sim \frac{r}{u_r} \sim \frac{1}{A} = \frac{\rho}{\mathcal{L}\,\xi_\perp}, \tag{4.10}$$

independent of r. At $r = L_c$, (2.2) and (4.9) match by construction.

The spectrum corresponding to (4.9) follows for a locally self-similar spectrum from the standard bridge $u_r^2 \sim \int_k^\infty E(q)\,\mathrm{d}q \simeq k\,E(k)$ with $k \sim 1/r$. Since $u_r^2 \sim A^2 r^2$, we obtain

$$E(k) \sim \left(\frac{\xi_\perp \mathcal{L}}{\rho}\right)^2 k^{-3}, \quad k_c \ll k \ll k_{\eta,fib}, \tag{4.11}$$

where $k_c \sim 1/L_c$ is the crossover wavenumber, and $k_{\eta,fib}$ denotes the effective dissipative cut-off in the fibre-dominated regime. Thus a k^{-3} subrange is attached to the K41 $k^{-5/3}$ branch at k_c.

https://doi.org/10.1017/jfm.2026.12044 Published online by Cambridge University Press

We now check *a posteriori* that neglecting viscosity is self-consistent for r between L_c and a new viscous scale $\eta_{fib} \sim 1/k_{\eta,fib}$. In the presence of both drag and viscosity, the scale-by-scale energy balance can be written schematically as

$$\frac{u_r^3}{r} \sim \varepsilon_{fib}(r) + \varepsilon_\nu(r), \quad \varepsilon_{fib}(r) \sim A u_r^2, \quad \varepsilon_\nu(r) \sim \nu \left(\frac{u_r}{r}\right)^2. \tag{4.12}$$

Inserting the fibre-dominated scaling $u_r \sim Ar$ from (4.9) gives

$$\varepsilon_{fib}(r) \sim A^3 r^2, \quad \varepsilon_\nu(r) \sim \nu A^2. \tag{4.13}$$

The scale η_{fib} at which viscous effects become comparable to fibre drag is obtained by equating the two contributions in (4.13):

$$A^3 \eta_{fib}^2 \sim \nu A^2 \quad \Longrightarrow \quad \eta_{fib} \sim \left(\frac{\nu}{A}\right)^{1/2} = \left(\frac{\nu\rho}{\xi_\perp \mathcal{L}}\right)^{1/2}. \tag{4.14}$$

For scales r such that $\eta_{fib} \ll r \ll L_c$, one has

$$\frac{\varepsilon_\nu(r)}{\varepsilon_{fib}(r)} \sim \frac{\nu A^2}{A^3 r^2} \sim \left(\frac{\eta_{fib}}{r}\right)^2 \ll 1, \tag{4.15}$$

and the viscous contribution is indeed sub-leading compared with fibre drag. For $r \lesssim \eta_{fib}$, the inequality is reversed, and viscous dissipation takes over, terminating the $u_r \propto r$ regime, and producing a dissipative tail. No additional asymptotic power-law regime is expected there; rather, one should anticipate a smooth crossover region around $r \sim \eta_{fib}$ where drag and viscous effects are comparable. In spectral space, this corresponds to a rounded transition from the k^{-3} branch to the final dissipative decay (typically, a stretched-exponential decay for $k \gtrsim k_{\eta,fib} \sim 1/\eta_{fib}$), rather than to a second distinct scaling range.

It is convenient to express η_{fib} in terms of the unladen Kolmogorov scale $\eta \sim (\nu^3/\varepsilon)^{1/4}$. Using (4.14), one finds

$$\frac{\eta_{fib}}{\eta} \sim \left(\frac{\varepsilon}{\nu}\right)^{1/4} \left(\frac{\rho}{\xi_\perp \mathcal{L}}\right)^{1/2} \equiv St_\eta^{-1/2}, \tag{4.16}$$

where $St_\eta \equiv (\xi_\perp \mathcal{L}/\rho)\,\tau_\eta$ is the small-scale Stokes number, and $\tau_\eta = (\nu/\varepsilon)^{1/2}$ is the Kolmogorov time scale.

The condition for a non-empty fibre-dominated band $\eta_{fib} \ll L_c$ is equivalent to $A \ll (\varepsilon/\nu)^{1/2}$, which, via (4.8), translates into the constraint $\mathcal{L} \ll (\varepsilon/\nu)^{1/2}(\rho/\xi_\perp)$, or, equivalently, into $\eta_{fib}/\eta \gg 1$. Under this constraint the dissipative cut-off is shifted from η to the larger scale η_{fib}, and there exists a finite interval

$$\eta_{fib} \ll r \ll L_c \quad \Longleftrightarrow \quad k_c \ll k \ll k_{\eta,fib} \tag{4.17}$$

in which the scale-by-scale balance between inertial transfer and fibre drag yields the $u_r \propto r$ and $E(k) \propto k^{-3}$ scalings derived above.

5. The QS consistency in the fibre-dominated frictional regime

The following estimates are meant within the overdamped Euler–Bernoulli/RFT framework adopted throughout the paper, where fibre inertia is negligible, and particle–particle interactions do not set the structural time scale. This last condition excludes regimes controlled by persistent contacts, flocculation, entanglement or jamming: the suspension is dynamically dense through hydrodynamic back-reaction, but mechanically

https://doi.org/10.1017/jfm.2026.12044 Published online by Cambridge University Press

unentangled. The Darcy-type term $-\alpha \boldsymbol{u}$, with $\alpha = \xi_\perp \mathcal{L}/\rho$, introduced in § 4 is a coarse-grained force density acting on the carrier flow; it is not a structural drag coefficient for an individual bending mode, and therefore does not replace the local transverse drag entering the single-fibre bending time.

With this restriction, we verify that the fibres remain in the QS regime in the new subrange $L \ll L_c$. The bending time is unchanged,

$$\tau_b(L) \sim \frac{\xi_\perp L^4}{\gamma}, \tag{5.1}$$

while the eddy correlation time is now $\tau_L^{fib} \sim 1/A$, independent of L; see (4.10). The QS condition $\tau_L^{fib} \gg \tau_b(L)$ becomes

$$\frac{1}{A} \gg \frac{\xi_\perp L^4}{\gamma} \quad \Leftrightarrow \quad L^4 \ll \frac{\rho\,\gamma}{\xi_\perp^2\,\mathcal{L}}. \tag{5.2}$$

The ratio $\tau_L^{fib}/\tau_b(L)$ decreases with increasing L, so the most stringent condition is at the upper edge $L = L_c$. If

$$L_c^4 \ll \frac{\rho\gamma}{\xi_\perp^2 \mathcal{L}} \quad \text{or} \quad \mathcal{L} \gg \left(\frac{\varepsilon^2 \rho^5}{\gamma \xi_\perp^4}\right)^{1/5}, \tag{5.3}$$

then the fibre is QS at $L = L_c$, and the inequality $\tau_L^{fib} \gg \tau_b(L)$ holds even more strongly for all $L < L_c$. Since by construction we choose parameters such that the fibres lie in the QS branch of the K41 regime (see (2.4)), the additional requirement (5.3) simply translates to selecting a total fibre length density $\mathcal{L}$ sufficiently high to satisfy the lower limit (5.3) for $\mathcal{L}$. Requiring that the upper bound on $\mathcal{L}$ be larger than the corresponding lower bound yields the condition $\gamma > \gamma_c \equiv \nu^{5/2}\,\xi_\perp/\varepsilon^{1/2}$.

6. Curvature scaling and hazard in the fibre-dominated regime

We now return to the fibre and set the scale r equal to the fibre span L. In the fibre-dominated regime $L \ll L_c$, the QS curvature scaling (2.3),

$$\kappa(L) \sim \frac{\xi_\perp}{\gamma}\, u_L\, L^2, \tag{6.1}$$

where, consistently with (2.3), $\kappa(L)$ is again understood as a characteristic midspan/peak curvature amplitude, combined with (4.9) gives

$$\kappa_{fib}(L) \sim \frac{\xi_\perp}{\gamma} A L^3 \sim \frac{\xi_\perp^2 \mathcal{L}}{\rho\gamma} L^3, \quad (\kappa L)_{fib} \sim \frac{\xi_\perp^2 \mathcal{L}}{\rho\gamma} L^4. \tag{6.2}$$

Compared with the drag-perturbed K41 QS scaling (2.3), the exponent in L changes from $7/3$ to 3. At the cut-off L_c, the two expressions coincide by construction, so the curvature amplitude is continuous across the crossover.

In the supercritical regime $\kappa_b \lesssim \kappa_{fib}(L)$, the hazard is controlled by the inverse correlation time (2.12). Using (4.10), we obtain

$$h_{fib}(L) \sim \frac{1}{\tau_r^{fib}} \sim A \sim \frac{\xi_\perp}{\rho}\mathcal{L}, \quad L \ll L_c,\ \kappa_b \lesssim \kappa_{fib}(L). \tag{6.3}$$

Thus in the fibre-dominated subrange, the supercritical hazard becomes independent of L, forming a plateau set solely by the global length density and drag. Because the present

https://doi.org/10.1017/jfm.2026.12044 Published online by Cambridge University Press

work is restricted to the supercritical regime, intermittency corrections are sub-leading for the leading-order hazard scalings in both (2.12) and (6.3): typical fluctuations are already sufficient to reach curvatures above the breaking threshold. By contrast, in the subcritical regime, not considered here, the hazard is controlled by rare events in the tails of the statistics, and intermittency becomes essential; see Mazzino (2026*a*).

7. Support from available numerical and experimental evidence

Before proceeding to the study of fragmentation kinetics, it is useful to discuss the numerical and experimental evidence presently available that can corroborate and, on the carrier-flow side, already quantitatively support the theoretical picture outlined above. We stress from the outset that a systematic validation of the present framework, and in particular a dedicated collapse test of the scaling laws (4.5), would require dedicated, fully coupled simulations of nearly neutrally buoyant slender fibres in a sufficiently extended inertial range, with enough statistical convergence to resolve simultaneously the carrier-flow crossover, the fibre deformation and the associated curvature statistics. Including fragmentation would make the task even more demanding, since each breaking event would require a topological update of the dispersed phase, the generation of daughter fibres and their renewed coupling to the carrier flow. Such simulations are computationally demanding and are beyond the scope of the present paper. At the same time, the absence of such a dedicated campaign does not mean that the theory is left without quantitative support. In the following, we report first quantitative evidence that confirms the carrier-flow side of the present framework: the QS-compatible fully coupled DNS of Olivieri *et al.* (2022) reproduce the predicted ordering and placement of the crossover across the nearly iso-dense cases, and the long-fibre case exhibits a finite high-k interval consistent with the onset of the k^{-3} branch.

7.1. *The QS fibre response and span-L forcing in the inertial range*

A first important piece of evidence is provided by the DNS of Rosti *et al.* (2018), who consider a single flexible fibre freely moving in homogeneous isotropic turbulence with a span in the inertial range. Their analysis identifies dynamical regimes in which the fibre is slaved to the turbulent fluctuations. In particular, the critical bending rigidity obtained from the resonance condition between the elastic time and the eddy-turnover time at the fibre scale (their equation (3)) can be rewritten (using the present notation) as $\gamma_{crit}^{od} \sim \rho\nu L^{10/3}\varepsilon^{1/3}$, i.e. the same $L^{10/3}$ dependence that underlies the QS condition (2.4). Moreover, Rosti *et al.* (2018) also stated that their numerical simulations show that the fibre is slaved to turbulence in the regime where $\gamma \gg \gamma_{crit}^{od}$. This directly supports two assumptions used here: first, that in the QS branch the fibre is effectively slaved to the eddies of comparable span; second, that the relevant forcing entering (2.1) is the velocity increment across the fibre length.

A complementary confirmation is provided by Brizzolara *et al.* (2021), who combine fully resolved DNS and laboratory experiments to introduce fibre tracking velocimetry. Although the fibres are rigid, the regime relevant here is again the low-inertia one. Their figure 2 shows that for sufficiently small Stokes number, the tumbling time of a fibre of length L matches the eddy-turnover time at the same scale. Their figures 3 and 4 in DNS, and figures 7 and 8 in the experiments, show that the transverse velocity increments reconstructed from the two fibre ends reproduce the corresponding Eulerian two-point statistics. This corroborates the use of u_L and τ_L as the natural kinematic inputs for an inertial-range fibre of span L.

https://doi.org/10.1017/jfm.2026.12044 Published online by Cambridge University Press

7.2. *Single-fibre fluid–structure cut-offs in dilute turbulence*

In the dilute, one-way-coupled setting, available studies do support the existence of single-fibre fluid–structure scales that organise inertial-range deformation for fibres longer than the Kolmogorov scale. The experiments of Brouzet *et al.* (2014) show that the transition from rigid to flexible behaviour is controlled by a characteristic elastic length, obtained from a balance between turbulent power and bending power (their equation (6)), which in the present notation can be written as $\ell_e \sim \gamma^{1/4}(\rho^2\nu\varepsilon)^{-1/8}$, and is organised experimentally by their figure 2. This is not the collective cut-off L_c of the present theory, but it supports the broader idea that appreciable inertial-range deformation is governed by a fluid–structure length rather than by brittleness alone.

The experiments of Verhille & Bartoli (2016) reinforce this picture by reconstructing the full three-dimensional conformation of a flexible fibre in turbulence. Their tangent–tangent correlation function $C(\ell)$ (their equation (5)) depends on both the elastic length ℓ_e and the total fibre length L, showing that the deformation statistics are organised not only by elasticity, but also by the finite span of the object in a correlated turbulent flow. They further note that the short-distance behaviour of $C(\ell)$ can be used to estimate ℓ_e with order-one accuracy. In the present context, the point of contact is therefore useful: the forcing experienced by an inertial-range fibre cannot be viewed as an uncorrelated local bath, and single-fibre deformation is controlled by fluid–structure scales that persist well above the Kolmogorov length.

At this stage, it is useful to distinguish the various length scales entering the problem. The QS scale L_{QS} from (2.4) is a temporal criterion, obtained by comparing the bending-relaxation and eddy-turnover times. By contrast, the elastic length ℓ_e introduced in dilute one-way-coupled studies and the related persistence length L_p used for end-to-end statistics organise the onset and spatial correlation of deformation of an isolated fibre in a prescribed turbulent flow (Brouzet *et al.* 2014; Verhille & Bartoli 2016). The collective cut-off L_c by (4.5) answers a third question, namely where the carrier-flow cascade is modified by the cumulative drag of the suspension. These scales therefore need not coincide. In particular, one may have $L < L_c$ and yet fail to be in the QS branch if L is not also below L_{QS}; this is precisely why the additional condition (5.3) is required.

7.3. *Quantitative support from fully coupled DNS for the carrier-flow crossover*

The most relevant fully coupled evidence is provided by the DNS of Olivieri *et al.* (2022), which solve the fully coupled dynamics of finite-size flexible fibres in homogeneous isotropic turbulence. Since the present theory is formulated for the QS branch, only the subset of their simulations that remains turbulence-controlled should be used for comparison, namely the nearly iso-dense cases. Their regime maps (their figures 7 and 8) show that these cases belong to the overdamped/turbulence-controlled branch, whereas the denser-than-the-fluid cases enter an underdamped regime and are therefore not appropriate as a direct validation of the present QS scenario.

Within that QS-compatible subset, the comparison with the present theory is not merely qualitative, but quantitatively consistent in three complementary senses. First, their figure 2 shows that the back-reaction on the carrier flow is organised much more clearly by the suspension mass fraction than by the geometric parameter nc^3. This supports the present view that the crossover cannot be controlled by a single-fibre length alone, but must depend on a collective loading variable; in the present theory, this role is played by the total fibre length density $\mathcal{L}$ in (4.5).

Second, consider the three nearly iso-dense cases in panels 3(*a*,*c*,*e*) at intermediate bending stiffness and $N = 10^3$. In the notation of Olivieri *et al.* (2022), these correspond to

https://doi.org/10.1017/jfm.2026.12044 Published online by Cambridge University Press

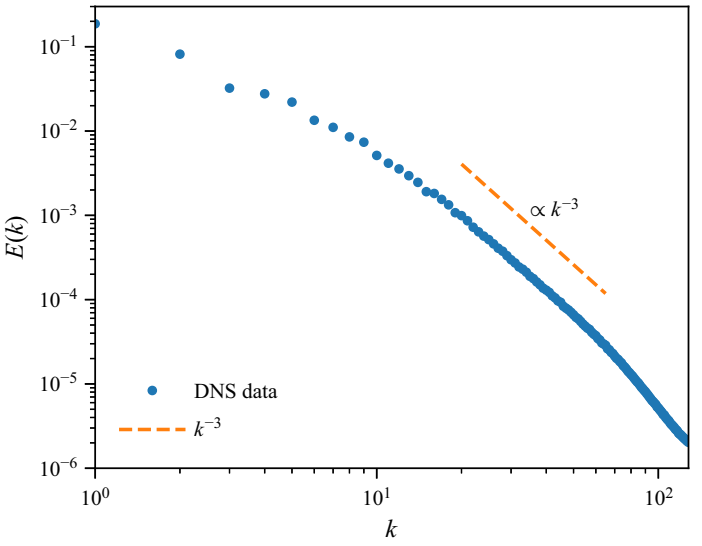


Figure 3. Log–log plot of the turbulent kinetic energy spectrum $E(k)$ (bullets) obtained from the DNS data of Olivieri *et al.* (2022), corresponding to (notation refers to this paper) the $N = 10^3$ curve in panel (*e*) of their figure 3, i.e. to the nearly iso-dense long-fibre case with $\Delta\tilde{\rho} = 10^{-3}$, $\gamma = 10^{-4}$. The dashed line is the k^{-3} reference slope.

the spans $c = 0.1, 0.5, 2.0$ in a triperiodic domain of volume $V = (2\pi)^3$. The associated monodisperse total fibre-length densities are therefore $\mathcal{L}^{(a)} = 10^3 \times 0.1/(2\pi)^3 \simeq 0.403$, $\mathcal{L}^{(c)} = 10^3 \times 0.5/(2\pi)^3 \simeq 2.016$, $\mathcal{L}^{(e)} = 10^3 \times 2.0/(2\pi)^3 \simeq 8.063$. At the level of a first scaling estimate, the dominant variation across the three cases is therefore carried by $\mathcal{L}$. Equation (4.5) then predicts $L_c^{(a)} : L_c^{(c)} : L_c^{(e)} \simeq 89 : 8 : 1$, where the superscripts refer to the panels of figure 3. Re-analysing the $N = 10^3$ curve from panel (*e*), reproduced here in figure 3, places the onset of the k^{-3} branch at $k_c^{(e)} \sim 10{-}20$, $k_c \sim L_c^{-1}$, which in turn implies $k_c^{(c)} \sim 1.3{-}2.5$, $k_c^{(a)} \sim 0.1{-}0.2$. Since in their DNS the forcing acts only in the band $1 \leq k \leq 2$, this means that the short-fibre case has its crossover below the forcing range, the intermediate case only at its edge, and only the long-fibre case places the crossover well inside the resolved inertial/high-k interval. This quantitatively explains why panels (*a*) and (*c*) remain almost indistinguishable from the fibre-free Kolmogorov spectrum, whereas panel (*e*) develops a distinct ultraviolet branch.

Moreover, the re-analysed $N = 10^3$ curve in figure 3 exhibits, before the final dissipative roll-off, a finite interval approximately $20 \lesssim k \lesssim 65$ that is well aligned with a k^{-3} guide to the eye. In the present framework, this is precisely the behaviour expected once the collective crossover has entered the inertial range.

Third, their scale-by-scale budget $P(k) + \Pi(k) + \Pi_{fs}(k) + D(k) = \varepsilon$ (see their equation (3.1)), shows the same ordering. In figure 5(*a*), the fluid–solid transfer $\Pi_{fs}(k)$ is negligible with respect to the nonlinear flux $\Pi(k)$; in figure 5(*c*), it is still only a modest correction; in figure 5(*e*), it becomes a non-negligible $O(1)$ contribution over an intermediate-to-high-k interval, while the nonlinear flux is correspondingly weakened. At the level of scaling, this is the Fourier space manifestation of the same crossover mechanism encoded here by (4.5). Although $\Pi_{fs}(k)$ is not the literal Fourier transform of the effective drag power used in the present closure, the ordering across panels (*a*,*c*,*e*) and the placement of the onset are quantitatively consistent with the estimate above.

https://doi.org/10.1017/jfm.2026.12044 Published online by Cambridge University Press

Taken together, these comparisons show that the DNS of Olivieri *et al.* (2022) provide a quantitative corroboration of the present picture. In the QS-compatible branch, they already provide a first quantitative support for the collective-crossover scenario: they identify the correct control variable, they reproduce the predicted monotonic decrease of L_c as the total fibre length density is increased, and they place the crossover below the observable inertial range in panel (*a*), only marginally at the forcing edge in panel (*c*), but clearly inside the resolved inertial/high-k interval in panel (*e*), exactly where a finite k^{-3} branch appears. What is still missing is not the existence of quantitative support, but rather a dedicated parameter sweep specifically designed to collapse the absolute prefactor and exponent of (4.5), and, beyond that, to test together (4.11) and the fragmentation-side predictions in the same fully coupled setting that we will analyse in the next section.

8. Fragmentation kinetics: drag-perturbed versus fibre-dominated regimes

We now sketch how the change in hazard scaling induced by collective fibre drag translates into different steady spectra for the fibre lengths. We work at the level of scalings, using a standard binary fragmentation equation with a scale-invariant kernel (Ziff & McGrady 1985; Krapivsky & Ben-Naim 1994; Domokos *et al.* 2015; Brouzet *et al.* 2021; Mazzino 2026*b*). The kinetic discussion is based on a minimal binary fragmentation closure appropriate to the QS/overdamped regime considered here, where fibre inertia is negligible, and post-break relaxation waves are expected to be strongly damped. We do not claim that correlated secondary break-up events are absent in all circumstances; rather, the scaling results below should be understood as the asymptotic prediction of this closure. A quantitative assessment of possible deviations, especially at very low breaking thresholds, would require dedicated simulations or experiments with explicit fracture dynamics.

To the best of our knowledge, no published DNS or experimental data set presently resolves this same QS, dynamically dense regime together with explicit break-up and the subsequent re-coupling of daughter fibres to the modulated carrier flow. The predictions discussed in this section should therefore be read as asymptotic targets for a dedicated future validation campaign.

Accordingly, the kinetic construction below should be read as a steady-state consistency argument at the level of scaling, rather than as a fully closed time-dependent model for the transient approach to stationarity. The detailed injection and removal mechanisms are only assumed to act near the large- and small-scale cut-offs while maintaining $\mathcal{L}$ statistically steady; the interior exponents predicted below are therefore not expected to depend on those details. By contrast, the transient dynamics and the linear or nonlinear stability of the stationary state are beyond the scope of the present asymptotic treatment.

8.1. *Binary kernel and steady scaling*

At the kinetic level, we describe fragmentation in terms of the number density $n(L)$ of fibres of span L and a hazard (breaking rate) $h(L)$. In a stationary self-similar range away from injection and dissipation cut-offs, it is natural to look for power laws

$$h(L) \sim L^{\beta}, \quad n(L) \sim L^{-\tau}, \tag{8.1}$$

with exponents β and τ. In the binary fragmentation framework developed in Mazzino (2026*b*), where break-up is described by a scale-invariant, length-conserving kernel, it is shown that a steady power-law spectrum exists only if the exponents satisfy

$$\tau = \beta + 2. \tag{8.2}$$

https://doi.org/10.1017/jfm.2026.12044 Published online by Cambridge University Press

This relation is universal for all length-conserving scale-invariant binary kernels considered in Mazzino (2026*b*): the detailed daughter-length distribution affects only order-one prefactors, not the exponent. In what follows, the turbulent flow enters solely through the hazard exponent β; once $h(L)$ is known in a given flow regime, the corresponding steady-spectrum exponent τ follows immediately from (8.2).

8.2. *Scaling exponents in the two regimes*

The supercritical hazards derived above can now be matched to the scaling ansatz (8.1), with the relation (8.2) between β and τ.

In the drag-perturbed regime, (2.12) gives $h_0(L) \sim \varepsilon^{1/3} L^{-2/3}$, so that

$$\beta_0 = -\frac{2}{3} \quad \Longrightarrow \quad \tau_0 = \beta_0 + 2 = \frac{4}{3}, \tag{8.3}$$

and the steady spectrum scales as $n_0(L) \propto L^{-4/3}$ in the K41 drag-perturbed regime.

In the fibre-dominated regime, the supercritical hazard plateau (6.3) implies $h_{fib}(L) \sim A \sim (\xi_\perp/\rho)\,\mathcal{L}$, i.e.

$$\beta_{fib} = 0 \quad \Longrightarrow \quad \tau_{fib} = \beta_{fib} + 2 = 2, \tag{8.4}$$

so that the steady spectrum in the fibre-dominated band $\eta_{fib} \ll L \ll L_c$ obeys $n_{fib}(L) \propto L^{-2}$. We stress that this prediction is claimed only inside the asymptotic interval $\eta_{fib} \ll L \ll L_c$, where the carrier-flow increment obeys $u_L \sim AL$, and the QS condition remains satisfied; no extension to arbitrarily small fibres is intended. The fibre-dominated spectrum is steeper than the 4/3 drag-perturbed regime, reflecting the span-independent breaking rate set by collective drag.

8.3. *Broken power law and physical picture*

Putting the two regimes together, a fragmentation cascade initiated at a large injection span L_{max} and evolving in a flow that becomes fibre-dominated below L_c is expected to develop a broken power-law spectrum

$$n(L) \propto \begin{cases} L^{-4/3}, & L_c \ll L \ll L_{max} \quad \text{(drag-perturbed band)}, \\ L^{-2}, & \eta_{fib} \ll L \ll L_c \quad \text{(fibre-dominated band)}. \end{cases} \tag{8.5}$$

The crossover at $L \sim L_c$ is controlled by the same length density $\mathcal{L}$ that sets the onset of the k^{-3} spectral range in the carrier flow. Increasing the fibre loading steepens both the velocity spectrum (by creating a k^{-3} band) and the fragment-size spectrum (by changing the hazard exponent from $-2/3$ to 0). Thus at the level of scaling, the fragmentation kinetics directly reflects the underlying change in the small-scale dynamics of the flow. Equation (8.5) should therefore be read as the asymptotic stationary prediction of the present binary QS closure. For a conceptually different route to nearby fragment-size exponents, based on maximal-randomness arguments rather than on a turbulence-controlled hazard, see Villermaux (2025).

8.4. *Self-consistency of the fragmentation cascade process*

We now ask whether the broken spectrum (8.5), together with the cut-off definition (4.5), is compatible with a statistically steady total length density. Specifically, we assume that injection of fibres at the largest span L_{max} and removal at small scales act so as to keep the total length density $\mathcal{L}$ approximately constant in time, and we check that this assumption is self-consistent given (8.5) and (4.5). The source/sink mechanism is not

https://doi.org/10.1017/jfm.2026.12044 Published online by Cambridge University Press

modelled microscopically here; it is only assumed to keep the system within the admissible window of $\mathcal{L}$ defined above, where the suspension remains volumetrically dilute, and the fibre-dominated band is non-empty.

The total fibre length per unit volume is given by (4.1). Using the two branches in (8.5) and splitting the integral at $L = L_c$ gives

$$\mathcal{L} \simeq \int_{\eta_{fib}}^{L_c} L\, n_{fib}(L)\, \mathrm{d}L + \int_{L_c}^{L_{max}} L\, n_0(L)\, \mathrm{d}L, \tag{8.6}$$

where $n_0(L) \propto L^{-\tau_0}$ with $\tau_0 = 4/3$ from the K41 drag-perturbed regime, and $n_{fib}(L) \propto L^{-\tau_{fib}}$ with $\tau_{fib} = 2$ from the fibre-dominated regime.

The contribution from the unladen band $L_c \ll L \ll L_{max}$ scales as

$$\int_{L_c}^{L_{max}} L\, n_0(L)\, \mathrm{d}L \propto \int_{L_c}^{L_{max}} L^{1-\tau_0}\, \mathrm{d}L = \int_{L_c}^{L_{max}} L^{-1/3}\, \mathrm{d}L \propto L_{max}^{2/3} - L_c^{2/3}, \tag{8.7}$$

and is therefore dominated by the largest spans as soon as $L_c \ll L_{max}$.

In the fibre-dominated band $\eta_{fib} \ll L \ll L_c$, we have the marginal exponent $\tau_{fib} = 2$. The corresponding contribution to $\mathcal{L}$ is

$$\int_{\eta_{fib}}^{L_c} L\, n_{fib}(L)\, \mathrm{d}L \propto \int_{\eta_{fib}}^{L_c} L^{1-\tau_{fib}}\, \mathrm{d}L = \int_{\eta_{fib}}^{L_c} \frac{\mathrm{d}L}{L} \propto \ln\!\left(\frac{L_c}{\eta_{fib}}\right), \tag{8.8}$$

which depends only logarithmically on the ratio L_c/η_{fib}. Even though the exponent $\tau_{fib} = 2$ is marginal, the dependence on the lower cut-off is very weak compared with the algebraic dependence on L_{max} in (8.7).

Thus in a statistically steady state where injection at L_{max} balances the outflow of total length, $\mathcal{L}$ is controlled primarily by the large-scale population, while the contribution of fragments with $L \ll L_{max}$ enters only through the weak logarithmic term.

Since the cut-off L_c depends on $\mathcal{L}$ via (4.5), this has an important implication: once the large-scale injection fixes $\mathcal{L}$, the value of L_c is set mainly by the longest fibres, and the progressive filling of the fibre-dominated band $\eta_{fib} \ll L \ll L_c$ does not feed back strongly on L_c. The cascade picture is therefore internally consistent.

9. Conclusions and outlook

We have developed a self-consistent kinetic description of fibre fragmentation in dense fibre-laden turbulence. Starting from an Euler–Bernoulli model in the quasi-static (QS) regime, we showed how the total fibre length density controls both the carrier flow and the fragmentation kinetics. When the length density is sufficiently large, the collective drag generates a cut-off scale L_c within the inertial range: for separations $L_c \ll r \ll L_{inj}$, the flow remains Kolmogorov-like but with an effective linear friction that reduces the energy flux, whereas for $\eta_{fib} \ll r \ll L_c$, the inertial transfer at each scale is locally balanced by drag power dissipated in fibre boundary layers. This small-scale balance produces velocity increments that grow linearly with r, a single friction time shared by all eddies in the fibre-dominated band, and a k^{-3} spectral subrange attached to the classical $k^{-5/3}$ branch. The carrier-flow part of this picture is supported quantitatively by the QS-compatible fully coupled DNS of Olivieri *et al.* (2022).

Within this frictional subrange, the QS curvature of an almost straight fibre grows as L^3, and the supercritical breaking hazard becomes independent of span, forming a plateau set solely by the global length density. In the drag-perturbed K41 regime, the hazard scales instead as $L^{-2/3}$, and the steady length spectrum is $\propto L^{-4/3}$. Embedding

https://doi.org/10.1017/jfm.2026.12044 Published online by Cambridge University Press

the fibre-dominated plateau into a scale-invariant, length-conserving binary fragmentation equation, we obtain as the asymptotic steady prediction of that closure a fibre-dominated spectrum $n(L) \propto L^{-2}$, with no adjustable parameters. The crossover between the $L^{-4/3}$ and L^{-2} branches is controlled by the same total length density that sets L_c and the onset of the k^{-3} range in the carrier flow. The same comparison with Olivieri *et al.* (2022) therefore gives quantitative support to the flow-side prediction of the theory, while the fragmentation-side consequences of that crossover, namely the span-independent supercritical hazard plateau and the associated steady branch $n(L) \propto L^{-2}$, should still be regarded as asymptotic predictions of the present QS binary closure.

The limitations of the present modelling approach are therefore precise. The theory assumes a coarse-grained, self-averaged fibre loading, rather than a contact network; it applies to mechanically unentangled suspensions in which particle–particle contacts, flocculation and jamming do not set the fibre relaxation time. It also assumes slender fibres whose relevant spans lie in the inertial/fibre-dominated range, with $\eta_{fib} \ll L \ll L_c$ for the $n(L) \propto L^{-2}$ branch, and which remain in the QS regime. Finally, the kinetic prediction relies on a supercritical, binary fragmentation closure; regimes controlled by subcritical rare events, correlated multi-break sequences or contact-mediated fracture require additional modelling.

The main perspective opened by the present work is therefore a dedicated validation of these fragmentation-side predictions. The relevant next step is fully coupled DNS or a purpose-built experiment in a regime where nearly neutrally buoyant slender fibres are simultaneously QS, dynamically dense, inertial-range, and allowed to undergo repeated breakage with consistent re-coupling of the daughter fibres to the carrier flow. Such a study would make it possible to test directly the predicted crossover from the drag-perturbed hazard $h(L) \propto L^{-2/3}$ to the fibre-dominated plateau, together with the associated transition from $n(L) \propto L^{-4/3}$ to $n(L) \propto L^{-2}$.

The present construction is deliberately minimal, and therefore flexible. A small-scale k^{-3} spectrum is also observed in other complex turbulent flows that host bubbles, drops or solid inclusions instead of fibres. With adjustments of the closure for drag or interfacial stresses, and relaxing the QS assumption for the fibre dynamics, our framework can be adapted to these systems as well, providing a natural candidate explanation for their observed small-scale k^{-3} regime.

Acknowledgements. Useful discussions with M.E. Rosti and S. Olivieri are acknowledged.

Declaration of interests. The authors report no conflict of interest.

References

ALLENDE, S., HENRY, C. & BEC, J. 2018 Stretching and buckling of small elastic fibers in turbulence. *Phys. Rev. Lett.* **121** (15), 154501.

ALLENDE, S., HENRY, C. & BEC, J. 2020 Dynamics and fragmentation of small inextensible fibres in turbulence. *Phil. Trans. R. Soc. Lond. A* **378** (2175), 20190398.

BATCHELOR, G.K. 1970 Slender-body theory for particles of arbitrary cross-section in Stokes flow. *J. Fluid Mech.* **44**, 419–440.

BOUNOUA, S., BOUCHET, G. & VERHILLE, G. 2018 Tumbling of inertial fibers in turbulence. *Phys. Rev. Lett.* **121** (12), 124502.

BRIZZOLARA, S., ROSTI, M.E., OLIVIERI, S., BRANDT, L., HOLZNER, M. & MAZZINO, A. 2021 Fiber tracking velocimetry for two-point statistics of turbulence. *Phys. Rev. X* **11** (3), 031060.

BROUZET, C., GUINÉ, R., DALBE, M.-J., FAVIER, B., VANDENBERGHE, N., VILLERMAUX, E. & VERHILLE, G. 2021 Laboratory model for plastic fragmentation in the turbulent ocean. *Phys. Rev. Fluids* **6** (2), 024601.

BROUZET, C., VERHILLE, G. & LE GAL, P. 2014 Flexible fiber in a turbulent flow: a macroscopic polymer. *Phys. Rev. Lett.* **112**, 074501.

https://doi.org/10.1017/jfm.2026.12044 Published online by Cambridge University Press

CHIARINI, A., ROSTI, M.E. & MAZZINO, A. 2024 Dynamics and applications of finite-size fibre-like objects in turbulent flows. *Eur. J. Mech. B/Fluids* **108**, 104–118.

COX, R.G. 1970 The motion of long slender bodies in a viscous fluid. Part 1. General theory. *J. Fluid Mech.* **44**, 791–810.

DERAKHSHANDEH, B., KEREKES, R.J., HATZIKIRIAKOS, S.G. & BENNINGTON, C.P.J. 2011 Rheology of pulp fibre suspensions: a critical review. *Chem. Engng Sci.* **66** (15), 3460–3470.

DERKANI, M.H., ALBERELLO, A., NELLI, F., BENNETTS, L.G., HESSNER, K.G., MACHUTCHON, K., REICHERT, K., AOUF, L., KHAN, S. & TOFFOLI, A. 2021 Wind, waves, and surface currents in the Southern Ocean: observations from the Antarctic Circumnavigation Expedition. *Earth Syst. Sci. Data* **13** (3), 1189–1209.

DOMOKOS, G., KUN, F., SIPOS, A.A. & SZABÓ, T. 2015 Universality of fragment shapes. *Sci. Rep.* **5**, 9147.

FRISCH, U. 1995 *Turbulence: The Legacy of A.N. Kolmogorov*. Cambridge University Press.

GAY, A., FAVIER, B. & VERHILLE, G. 2018 Characterisation of flexible fibre deformations in turbulence. *Europhys. Lett.* **123** (2), 24001.

KEREKES, R.J. & SCHELL, C.J. 1992 Characterization of fibre flocculation regimes by a crowding factor. *J. Pulp Paper Sci.* **18**, 32–38.

KHAN, M., AGRAWAL, P., STEINBERG, V. & SHAQFEH, E.S.G. 2023 A constitutive model for sheared dense fiber suspensions. *Phys. Fluids* **35** (1), 013337.

KIM, S. & KARRILA, S.J. 1991 *Microhydrodynamics: Principles and Selected Applications*. Butterworth–Heinemann.

KOLMOGOROV, A.N. 1941 The local structure of turbulence in incompressible viscous fluid for very large Reynolds numbers. *Dokl. Akad. Nauk SSSR* **30**, 301–305.

KRAPIVSKY, P.L. & BEN-NAIM, E. 1994 Scaling and multiscaling in models of fragmentation. *Phys. Rev. E* **50** (5), 3502–3507.

LUNDELL, F., SÖDERBERG, L.D. & ALFREDSSON, P.-H. 2011 Fluid mechanics of papermaking. *Annu. Rev. Fluid Mech.* **43**, 195–217.

MARCHIOLI, C., ROSTI, M.E. & VERHILLE, G. 2026 Flexible fibers in turbulence. *Annu. Rev. Fluid Mech.* **58**, 167–192.

MAZZINO, A. 2026*a* Intermittency-driven subcritical fiber breakage in turbulence. *Phys. Rev. Res.* **8**, 033073.

MAZZINO, A. 2026*b* Turbulence-informed kinetic theory of inertial-range fibre fragmentation. *J. Fluid Mech.* **1030**, A6.

MAZZINO, A. & SUARIA, G. 2026 Sea-surface retention effect shapes ocean microplastic fibers. *Phys. Rev. Res.* **8**, 023283.

OLIVIERI, S., AKOUSH, A., BRANDT, L., ROSTI, M.E. & MAZZINO, A. 2020*a* Turbulence in a network of rigid fibers. *Phys. Rev. Fluids* **5** (7), 074502.

OLIVIERI, S., BRANDT, L., ROSTI, M.E. & MAZZINO, A. 2020*b* Dispersed fibers change the classical energy budget of turbulence via nonlocal transfer. *Phys. Rev. Lett.* **125** (11), 114501.

OLIVIERI, S., MAZZINO, A. & ROSTI, M.E. 2022 On the fully coupled dynamics of flexible fibres dispersed in modulated turbulence. *J. Fluid Mech.* **946**, A34.

OLSON, J.A. & KEREKES, R.J. 1998 The motion of fibres in turbulent flow. *J. Fluid Mech.* **377**, 47–64.

PARSA, S. & VOTH, G.A. 2014 Inertial range scaling in rotations of long rods in turbulence. *Phys. Rev. Lett.* **112**, 024501.

ROSTI, M.E., BANAEI, A.A., BRANDT, L. & MAZZINO, A. 2018 Flexible fiber reveals the two-point statistical properties of turbulence. *Phys. Rev. Lett.* **121** (4), 044501.

DU ROURE, O., LINDNER, A., NAZOCKDAST, E.N. & SHELLEY, M.J. 2019 Dynamics of flexible fibers in viscous flows and fluids. *Annu. Rev. Fluid Mech.* **51**, 539–572.

RYAN, P.G., SUARIA, G., PEROLD, V., PIERUCCI, A., BORNMAN, T.G. & ALIANI, S. 2020 Sampling microfibres at the sea surface: the effects of mesh size, sample volume and water depth. *Environ. Pollut.* **258**, 113413.

SINGH, R.K., PICARDO, J.R. & RAY, S.S. 2022 Sedimenting elastic filaments in turbulent flows. *Phys. Rev. Fluids* **7** (8), 084502.

SUARIA, G., PEROLD, V., LEE, J.R., LEBOUARD, F., ALIANI, S. & RYAN, P.G. 2020*a* Floating macro- and microplastics around the Southern Ocean: results from the Antarctic Circumnavigation Expedition. *Environ. Intl* **136**, 105494.

SUARIA, G., PEROLD, V., LEE, J.R., LEBOUARD, F., ALIANI, S. & RYAN, P.G. 2020*b* Microfibers in oceanic surface waters: a global characterization. *Sci. Adv.* **6** (23), eaay8493.

VERHILLE, G. & BARTOLI, A. 2016 3D conformation of a flexible fiber in a turbulent flow. *Exp. Fluids* **57**, 117.

VILLERMAUX, E. 2025 Fragmentation: principles versus mechanisms. *Phys. Rev. Lett.* **135** (22), 228201.

ZIFF, R.M. & MCGRADY, E.D. 1985 The kinetics of cluster fragmentation and depolymerisation. *J. Phys. A: Math. Gen.* **18** (15), 3027–3037.

https://doi.org/10.1017/jfm.2026.12044 Published online by Cambridge University Press